

Si/Ge Double-Layered Nanotube Array as a Lithium Ion Battery Anode

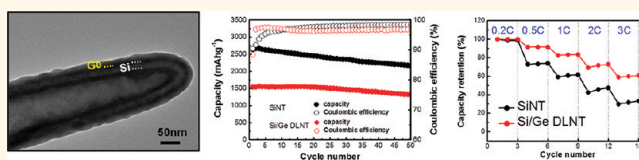
Taeseup Song,[†] Huanyu Cheng,[‡] Heechae Choi,[†] Jin-Hyon Lee,[†] Hyungkyu Han,[†] Dong Hyun Lee,[†] Dong Su Yoo,[†] Moon-Seok Kwon,[§] Jae-Man Choi,[§] Seok Gwang Doo,[§] Hyuk Chang,[§] Jianliang Xiao,[⊥] Yonggang Huang,[‡] Won Il Park,[†] Yong-Chae Chung,[†] Hansu Kim,^{||,*} John A. Rogers,^{⊥,*} and Ungyu Paik^{†,||,*}

[†]Department of Materials Science Engineering, Hanyang University, Seoul 133-791, Korea, [‡]Departments of Civil and Environmental Engineering and Mechanical Engineering, Northwestern University, Evanston, Illinois 60208, United States, [§]Energy Lab, Samsung Advanced Institute of Technology, Samsung Electronics Co. Ltd., Suwon 440-600, Korea, [⊥]Department of Materials Science and Engineering, University of Illinois at Urbana—Champaign, Urbana, Illinois 61801, United States, and, ^{||}WCU Department of Energy Engineering, Hanyang University, Seoul 133-791, Korea

Various types of one-dimensional nanostructures, including nanowires, nanobelts, and nanotubes, have been explored for applications, due to unique physical and chemical properties that result from their geometry and small dimension.^{1–5} Group IVA based nanomaterials such as Si nanowires and Ge nanowires are of particular interest for use in electronics, optics, sensors, and energy-related devices.^{6,7} The concept of engineering both composition and geometry in IVA based nanowires has been used to modify their physicochemical properties and enhance their performance in devices.^{8,9} By contrast, nanotube heterostructures have received little attention, partly due to difficulties in synthesis, despite the potential to exploit their large surface areas and compositions for engineering the band gap and controlling the interface properties. In previous studies, we demonstrated that Si nanotubes offer desirable architectures for accommodating large volume change associated with lithiation in a reversible manner to offer improved cycle retention and reliable operation of lithium ion batteries.¹⁰ A remaining disadvantage of this system is that it requires high-power-rate properties, due to the inherently low electron conductivity and ion diffusivity of silicon. Balanced battery design in both energy density and power density is essential to the critical applications such as large-scale storage for renewable power sources, electric vehicles, and plug-in hybrid electric vehicles.

Here, we report vertically aligned group IVA based nanotube heterostructure arrays by employing a template-assisted synthesis method based on chemical vapor deposition process. With optimal designs, Si/Ge double-layered nanotubes (Si/Ge DLNTs) can serve as an anode for lithium ion batteries

ABSTRACT



Problems related to tremendous volume changes associated with cycling and the low electron conductivity and ion diffusivity of Si represent major obstacles to its use in high-capacity anodes for lithium ion batteries. We have developed a group IVA based nanotube heterostructure array, consisting of a high-capacity Si inner layer and a highly conductive Ge outer layer, to yield both favorable mechanics and kinetics in battery applications. This type of Si/Ge double-layered nanotube array electrode exhibits improved electrochemical performances over the analogous homogeneous Si system, including stable capacity retention (85% after 50 cycles) and doubled capacity at a 3C rate. These results stem from reduced maximum hoop strain in the nanotubes, supported by theoretical mechanics modeling, and lowered activation energy barrier for Li diffusion. This electrode technology creates opportunities in the development of group IVA nanotube heterostructures for next generation lithium ion batteries.

KEYWORDS: silicon · germanium · nanotubes · anode · lithium ion batteries

to enable improvements in structural stability and electrochemical kinetics. On the basis of their mechanical and electrochemical properties, Si and Ge were selected as inner and outer material layers, respectively. This strategy minimizes both the mechanical stress applied to the inner layer (Si shell) during lithiation and the electrochemical resistance. The latter is obtained because Ge has higher electrical conductivity (4 orders of magnitude) and lithium ion diffusivity (2 orders of magnitude) and smaller volume change during cycling than Si.^{11,12} Calculations show that the maximum hoop strain in Si/Ge DLNT can be reduced compared to that in homogeneous Si nanotubes (SiNTs). The rate capability benefits

* Address correspondence to khansu@hanyang.ac.kr, jrogers@illinois.edu, upaik@hanyang.ac.kr.

Received for review September 16, 2011 and accepted December 5, 2011.

Published online December 05, 2011
10.1021/nn203572n

© 2011 American Chemical Society

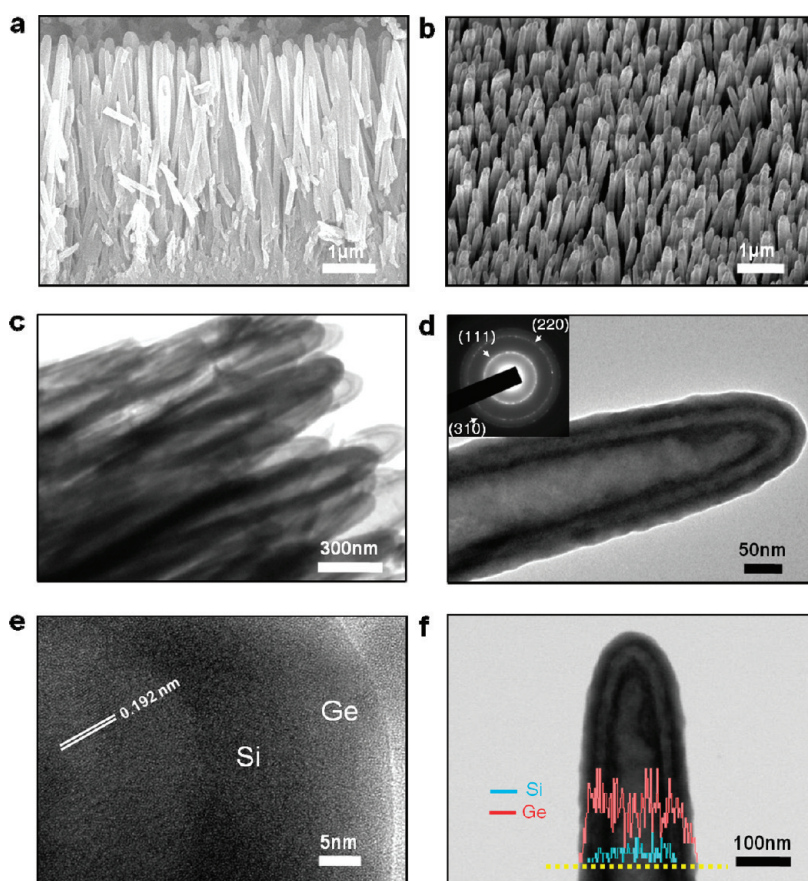


Figure 1. Electron microscope images and elemental line profile analysis of Si/Ge DLNT. Cross sectional (a) and 45° tilted (b) SEM images of a vertically aligned Si/Ge DLNT array on a stainless steel substrate. Low- (c) and high- (d) magnification TEM images of the Si/Ge DLNT. Inset of (d) shows selective area electron diffraction pattern. (e) High-resolution TEM image of Si/Ge DLNT at the interface between Si and Ge. (f) Cross-sectional EDX elemental mapping along the yellow dotted line. Light blue and red lines indicate Si and Ge, respectively.

from the growth of the anode structure directly on the current collector to provide efficient and fast pathways for electron transport. The resulting improvements in electrochemical performance over the homogeneous analogue are significant.

RESULTS AND DISCUSSION

Figure 1 provides electron microscopy images and elemental analysis of a radially controlled Si/Ge DLNT. Scanning electron microscopy (SEM) and low-magnification transmission electron microscopy (TEM) images show that the Si/Ge DLNT has a wall thickness of 30 nm, inner diameters of 60 nm near the tip of the tube, and the length of 4–5 μm . The morphologies and dimensions of Si/Ge DLNTs are similar to those of previously reported SiNTs.¹⁰ A uniform and smooth Ge shell layer with a thickness ranging from 10 to 15 nm is formed on the surface of a SiNT with a thickness ranging from 15 to 20 nm. The lattice-resolved TEM image and selective area electron diffraction (SAED) pattern reveal that the Si inner layer and the Ge shell layer are crystalline and amorphous, respectively, which is also supported by X-ray diffraction (XRD) and Raman and Auger

electron spectroscopy results (Figures S1–S3 in Supporting Information). Compositional line profiles clearly confirm the Si/Ge double-layered microstructure without any trace of Zn and O from the nanowire growth template.

The Si/Ge DLNT electrodes exhibit the first charge (lithium removal) of 1544.6 mAh g^{-1} and discharge capacities (lithium insertion) of 1746.1 mAh g^{-1} in the range of 0.01 and 2.0 V (vs Li/Li^+) at a rate of 0.2 C (Figure 2a), with an initial Coulombic efficiency (88.5%) that is much higher than those of previously reported Ge electrode such as mesoporous Ge particles, Ge thin film, and Ge nanowires and comparable to that of a carbon-layer-coated Ge nanowire electrode.^{13–16} This result implies that the initial Coulombic efficiency can be improved by tailoring electrode configuration without an additional protecting layer on the surface of the Ge. The Si/Ge DLNT array showed two distinct voltage plateaus in the discharge voltage profile shown in Figure 2a. The first voltage plateau, located between 0.2 and 0.4 V, corresponds to the alloying reaction of the Ge shell layer with lithium, as supported by TEM images of the microstructure and SAED patterns for

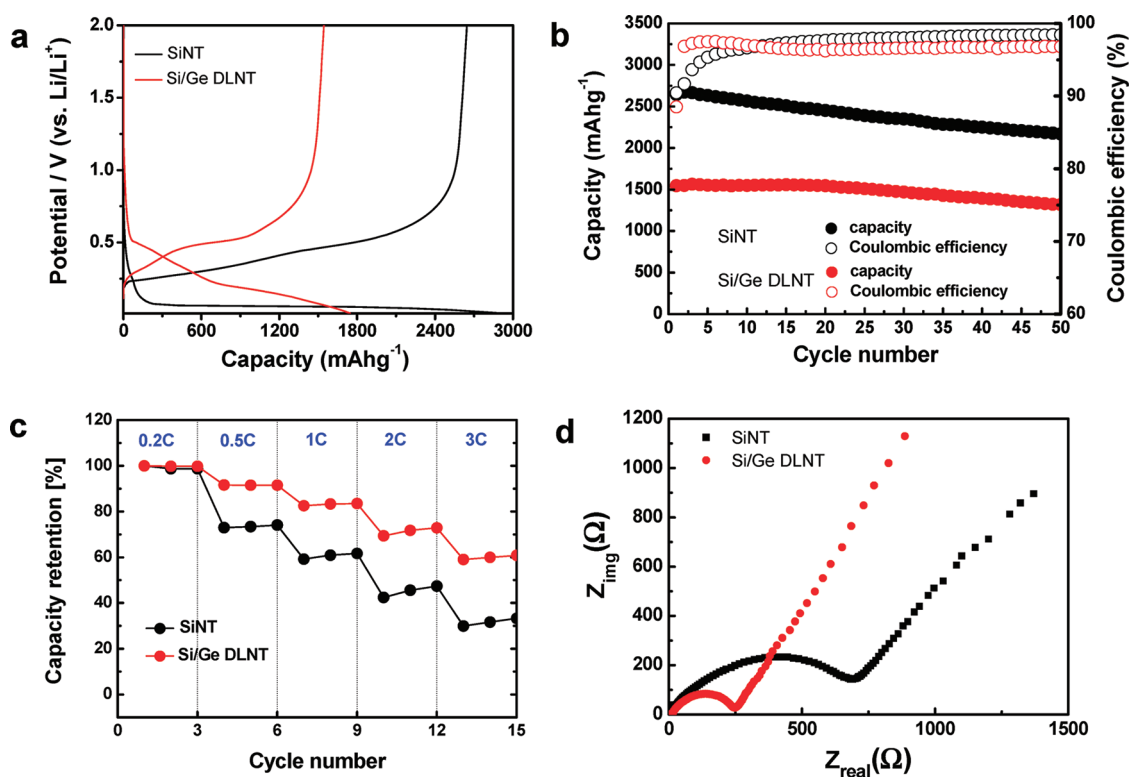


Figure 2. Electrochemical characteristics of both Si NT and Si/Ge DLNT array electrodes. (a) Voltage profiles of Si NT and Si/Ge DLNT for the first cycle at a rate of 0.2 C. (b) Cycle performances. (c) Rate capabilities of Si NT and Si/Ge DLNT array electrodes at various C rates. (d) Impedance plots for the Si NT and Si/Ge DLNT.

35% lithium inserted into the Si/Ge DLNT (see the Supporting Information). Another downward slope voltage plateau, located under 0.2 V, arises from the alloying reactions of both Ge and Si with lithium. A corresponding SiNT array anode exhibited the first charge of 2920 mAh g^{-1} and discharge capacities of 2640 mAh g^{-1} at a rate of 0.2 C. It should be noted that the Si/Ge DLNT electrode ($\sim 1.2 \text{ mAh cm}^{-2}$) has 2-fold higher areal capacity compared to that of the SiNT electrode ($\sim 0.6 \text{ mAh cm}^{-2}$), even though the SiNT array anode delivered 2-fold higher gravimetric capacity than that of the Si/Ge DLNT case. In addition, the Si/Ge DLNT electrode shows higher capacity retention (85%) at a rate of 0.2 C after 50 cycles compared to that of the SiNT (82%), suggesting that radially modulated Si/Ge DLNT improves the mechanics associated with the alloying and dealloying with Li. Mechanics modeling provides insights into the underlying physics of this process. We assumed that Si and Ge are fully reacted with Li, and lithiation in bulk Si and Ge gives volumetric expansion $\Delta V_{\text{Si}} = 400\%$ and $\Delta V_{\text{Ge}} = 370\%$, respectively. The smaller volumetric expansion in Ge leads to an additional compressive strain in the Si inner layer, thereby reducing the volume expansion (*i.e.*, $<400\%$) and net strain in the Si. This mechanics is likely responsible for the aforementioned capacity retention results. To explore in further details, let r_{Si} and r_{Ge} denote the inner radius of the Si inner layer and the

outer radius of the Ge shell layer before lithiation, respectively, and $r_{\text{interface}}$ represent the radius of the Si/Ge boundary. If the Si inner layer was isolated, its inner and outer radii r_{Si} and $r_{\text{interface}}$ would expand to $\Delta V_{\text{Si}}^{1/3} r_{\text{Si}}$ and $\Delta V_{\text{Si}}^{1/3} r_{\text{interface}}$, respectively. Similarly, an isolated Ge shell layer would expand its inner and outer radii to $\Delta V_{\text{Ge}}^{1/3} r_{\text{interface}}$ and $\Delta V_{\text{Ge}}^{1/3} r_{\text{Ge}}$, respectively. The outer radius of the Si inner layer $\Delta V_{\text{Si}}^{1/3} r_{\text{interface}}$ would be larger than the inner radius $\Delta V_{\text{Ge}}^{1/3} r_{\text{interface}}$ of the Ge shell layer since $\Delta V_{\text{Si}} > \Delta V_{\text{Ge}}$. This leads to pressure P at the Si/Ge interface in the lithiated Si/Ge DLNT. For a tube with inner and outer radii r_i and r_o subjected to internal pressure p_i and external pressure p_o , the displacement u_r in the radial direction is given by¹⁷

$$u_r = \frac{1}{E} \left[\frac{(1-\nu)(r_i^2 p_i - r_o^2 p_o)}{r_o^2 - r_i^2} r + \frac{(1+\nu)r_i^2 r_o^2 (p_i - p_o)}{r_o^2 - r_i^2} \frac{1}{r} \right] \quad (1)$$

where E and ν are Young's modulus and Poisson's ratio of the tube, and r is the distance from the tube axis. The displacement $(u_r)_{\text{Si}}$ at the outer radius of the Si inner layer due to pressure P is obtained from eq 1 by $r_i = \Delta V_{\text{Si}}^{1/3} r_{\text{Si}}$, $r = r_o = \Delta V_{\text{Si}}^{1/3} r_{\text{interface}}$, $p_i = 0$, and $p_o = P$. The displacement $(u_r)_{\text{Ge}}$ at the inner radius of the Ge shell layer due to pressure P is obtained by $r = r_i = \Delta V_{\text{Ge}}^{1/3} r_{\text{interface}}$, $r_o = \Delta V_{\text{Ge}}^{1/3} r_{\text{Ge}}$, $p_i = P$, and $p_o = 0$. Compatibility of displacements across the interface in the Si/Ge

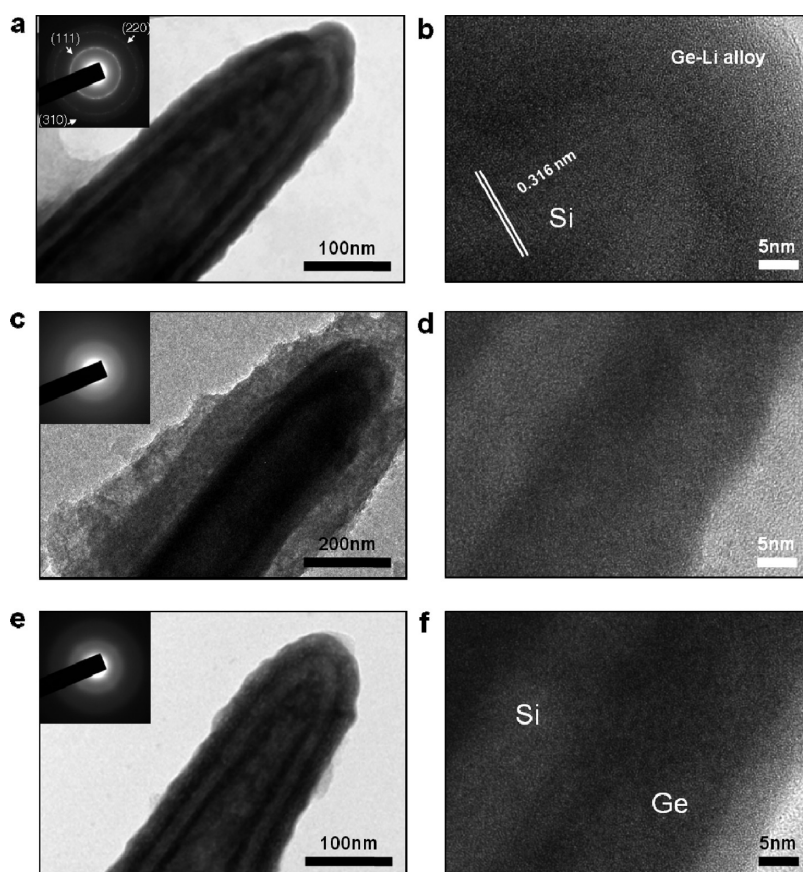


Figure 3. Electron microscopy images of Si/Ge DLNT as a function of an amount of lithium insertion. Microscopy shows the morphological changes during the first cycling. Low-magnification (a,c,e) and high-resolution (b,d,f) TEM images of 35% lithium inserted Si/Ge DLNT, fully lithiated Si/Ge DLNT, and delithiated Si/Ge DLNT, respectively.

DLNT requires $\Delta V_{\text{Si}}^{1/3} r_{\text{Si}} + (u_r)_{\text{Si}} = \Delta V_{\text{Ge}}^{1/3} r_{\text{Ge}} + (U_r)_{\text{Ge}}$ which gives the pressure at the interface

$$P = \left(\sqrt[3]{\Delta V_{\text{Si}}} - \sqrt[3]{\Delta V_{\text{Ge}}} \right) \left[\frac{\sqrt[3]{\Delta V_{\text{Si}}}}{E_{\text{Li}_{4.4}\text{Si}}} \left(\frac{r_{\text{interface}}^2 + r_{\text{Si}}^2}{r_{\text{interface}}^2 - r_{\text{Si}}^2} - \nu_{\text{Li}_{4.4}\text{Si}} \right) + \frac{\sqrt[3]{\Delta V_{\text{Ge}}}}{E_{\text{Li}_{4.4}\text{Ge}}} \left(\frac{r_{\text{Ge}}^2 + r_{\text{interface}}^2}{r_{\text{Ge}}^2 - r_{\text{interface}}^2} + \nu_{\text{Li}_{4.4}\text{Ge}} \right) \right] \quad (2)$$

where $E_{\text{Li}_{4.4}\text{Si}} = 15.2$ GPa and $\nu_{\text{Li}_{4.4}\text{Si}} = 0.328$ are the Young's modulus and Poisson's ratio of lithiated Si ($\text{Li}_{4.4}\text{Si}$),¹⁰ and $E_{\text{Li}_{4.4}\text{Ge}} = 15.6$ GPa and $\nu_{\text{Li}_{4.4}\text{Ge}} = 0.326$ for lithiated Ge ($\text{Li}_{4.4}\text{Ge}$) are obtained following the same approach.¹⁰ The distribution of (compressive) hoop strain in Si is given by $-(\Delta V_{\text{Si}})^{1/3} r_{\text{interface}}^2 P / (E_{\text{Li}_{4.4}\text{Si}} (r_{\text{interface}}^2 - r_{\text{Si}}^2)) [1 - \nu_{\text{Li}_{4.4}\text{Si}} + (1 + \nu_{\text{Li}_{4.4}\text{Si}}) r_{\text{Si}}^2 / r_{\text{interface}}^2]$.¹⁷ For $r_{\text{Si}} = 30$ nm, $r_{\text{interface}} = 45$ nm, $r_{\text{Ge}} = 60$ nm, as in experiments, this gives a compressive hoop strain of -1.55% at the interface and -2.45% at the inner surface of the Si inner layer. The strain in the radial direction is only -0.100% at the interface. The maximum compressive strain is then given by

$$\varepsilon = \frac{-2 \sqrt[3]{\Delta V_{\text{Si}}} r_{\text{interface}}^2 P}{E_{\text{Li}_{4.4}\text{Si}} (r_{\text{interface}}^2 - r_{\text{Si}}^2)} \quad (3)$$

Its absolute value (*i.e.*, $-\varepsilon$) is shown in Figure 4 as a function of the Si volume fraction, $(r_{\text{interface}}^2 - r_{\text{Si}}^2) / (r_{\text{Ge}}^2 - r_{\text{Si}}^2)$, in the un lithiated state (with $r_{\text{Si}} = 30$ nm and $r_{\text{Ge}} = 60$ nm). As the Si volume fraction decreases, the (absolute value of) maximum compressive strain increases. This reduces the total strain in Si (sum of tension due to lithiation and compression due to Ge shell layer confinement), thereby facilitating capacity retention. However, the total capacity of Si/Ge DLNT also decreases with Si volume fraction because Si has a higher specific capacity than Ge, as shown in Figure 4, where the total capacity of Si/Ge DLNT is normalized by its maximum value for pure Si (with the same inner and outer radii of 30 and 60 nm).

In addition to these mechanics aspects, the electrochemical kinetics can be significantly improved through modulating the composition of homogeneous SiNT with highly conductive material (Ge) in the radial direction. The Si/Ge DLNT electrode system delivers a charge capacity of 61% at the 3C rate, almost two times higher than that of SiNT electrode, which can be attributed to both fast electron conductivity and high Li ion diffusivity of Ge. As shown in Figure 2d, the Si/Ge DLNT electrode shows much lower impedance compared to that of the SiNT electrode, which is

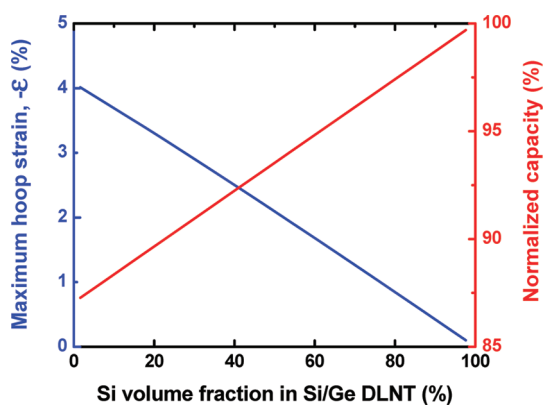


Figure 4. Maximum hoop strain $-\varepsilon$ (%) and normalized capacity (%) versus Si volume fraction in Si/Ge DLNT (%).

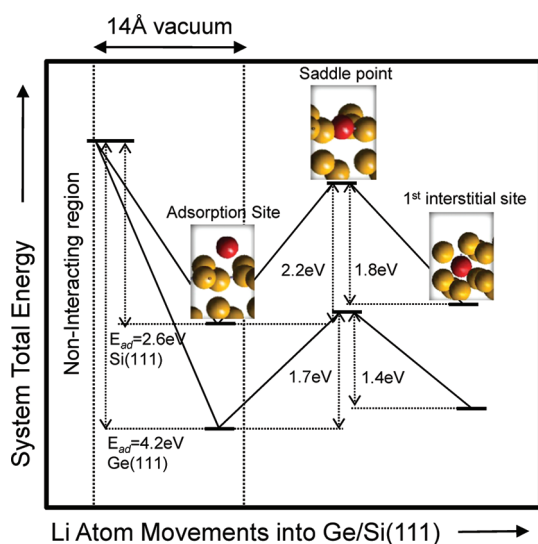


Figure 5. Plot of the system total energy change about to the Li movements into Ge(111) and Si(111). The yellow (red) sphere represents the substrate (Li) atoms.

consistent with the rate capability results of SiNT and Si/Ge DLNT electrodes. To yield insights into the origins of the enhanced electrochemical kinetics and to understand the role of the Ge shell layer, we performed density functional theory (DFT) calculations of a type which has been recently exploited to show the atomic movements in lithium ion battery anodes.^{18,19} The adsorption energies of the Li atom on Si(111) and Ge(111) surfaces, E_{ad} , were defined as $E_{\text{ad}} = E_{\text{Li/sub}} - (E_{\text{Li}} + E_{\text{sub}})$, where $E_{\text{Li/sub}}$, E_{Li} , and E_{sub} are the total energies of Li-adsorbed Si(111) and Ge(111), isolated Li atom, and the clean Si(111) and Ge(111) substrates. The adsorption energies of Li on Si(111) and Ge(111) surfaces were calculated to be 2.6 and 4.2 eV, respectively (Figure 5). Li adsorption on Ge(111) surfaces induces significant decreases in the system total energy compared to a case of Li on Si(111) surfaces, leading to more favorable kinetics. The calculated energy barrier for the diffusion of adsorbed Li atoms into the

first interstitial sites was 2.2 and 1.8 eV on Si(111) and Ge(111), respectively, as shown in Figure 5, implying that both higher adsorption energy and lower diffusion energy barriers of Li on Ge(111) contributes to enhanced electrochemical kinetics with the addition of Ge.

Further experiments revealed the structural morphology and changes in microstructure in three different samples of Si/Ge DLNT, each with a different amount of Li inserted: (i) 35% lithiated, (ii) fully lithiated, and (iii) fully delithiated (Figure 3). The first case shows structures with their original shapes and dimensions (Figure 3a). HR-TEM image (Figure 3b) and SAED pattern (inset of Figure 3a) confirm that the Si inner layer maintains its crystallinity, due to its relatively high applied lithiation potential (2–0.28 V; Figure S4). While the amorphous Ge reacts with lithium at the potential range from 0.4 to 0 V, the crystalline Si does not react with lithium until the applied voltage of 0.1 V for the first cycle. Therefore, only Ge reacts with lithium at these applied voltage ranges. Despite large volumetric expansion after the full lithiation, the Si/Ge DLNT retains its initial one-dimensional shape without mechanical degradation. XRD was employed to analyze the final products of lithiated Si/Ge DLNT. While Si is completely converted to the fully lithiated form ($\text{Li}_{22}\text{Si}_5$) as a final product, Ge has intermediate $\text{Li}_{11}\text{Ge}_6$ intermetallic phase as well as fully lithiated $\text{Li}_{22}\text{Ge}_5$ (Figure S5). The formation of the intermediate $\text{Li}_{11}\text{Ge}_6$ intermetallic phase is not yet clearly understood in the Si/Ge DLNT electrode. Further study will be carried out to clarify this point. The mechanics of Si/Ge DLNT with final products of $\text{Li}_{22}\text{Si}_5$, $\text{Li}_{22}\text{Ge}_5$, and $\text{Li}_{11}\text{Ge}_6$ in fully lithiated state was also investigated. Since it is difficult to obtain the exact volume expansion degree of Ge in the fully lithiated state, the maximum hoop strain in the Si/Ge DLNT is calculated as a function of the volume expansion degree of Ge in given dimension ($r_{\text{Si}} = 30$ nm, $r_{\text{Ge}} = 60$ nm, and $r_{\text{interface}} = 45$ nm) (Figure S6). The maximum hoop strain is significantly decreased with the volume expansion degree of Ge, which implies that the volume expansion behavior of our Si/Ge DLNT in a given system could provide more favorable mechanics. After the first full cycle, the swelled overall shell thickness and inner void space are reversibly restored to the initial state. HR-TEM image (Figure 3f) and SAED pattern (inset of Figure 3e) reveal that the crystalline phase of Si completely transforms into amorphous, which is consistent with the Raman result (Figure S7) and previous reports. More interestingly, the Si inner layer and Ge outer layer are completely recovered after subsequent volume contraction of Si and Ge (Figure S8). The Si/Ge DLNT array maintained their one-dimensional geometry without the delamination from the current collector after 50 cycles (Figure S9).

CONCLUSION

In conclusion, radially modulated group IVA nanotube arrays on metallic substrates offer underlying mechanics and kinetics that improve both cyclability and rate capability over previously reported homogeneous

SiNT arrays. The strategies presented here could provide important avenues for nanotube heterostructures in various applications not only in batteries but also in other systems of interest, ranging from electronics to photovoltaics.

EXPERIMENTAL DETAILS

A thin ZnO seed layer was deposited on 15 μm thick stainless steel substrate (Nilaco, Tokyo, Japan) with 12 mm diameter by radio frequency magnetron sputtering. An array of ZnO nanorods, which serve as templates for the nanotubes, was grown on the seed layer by a hydrothermal method at 85 $^{\circ}\text{C}$. Then, 0.025 M zinc nitrate hexahydrate and 0.025 M hexamethylenetetramine were used as precursor chemicals. A 15–20 nm thick Si shell layer was coated on the ZnO template by chemical vapor deposition (CVD), and then the ZnO template was selectively etched out. The detailed synthesis condition and procedure for SiNT growth are described in our previous report.¹⁰ The Ge outer layer was deposited on the SiNT array at 330 $^{\circ}\text{C}$, with a chamber pressure of 100 Torr, using germane gas (10% GeH_4 in a diluted in H_2) with flow rates of 30–50 sccm. Si/Ge DLNT arrays were characterized using a field emission scanning electron microscope (FE-SEM, S-4700, Hitachi, Japan), a field emission transmission electron microscope (FE-TEM, JEM 2100F, JEOL, Japan), an X-ray diffraction spectrometer (D/MAX-2500/PC, Rigaku, Japan), Auger electron spectroscopy (PHI 680, Physical Electronics, USA), and Raman spectroscopy (LabRam HR, Horiba Jobin-Yvon, France).

Coin-type half cells (2016R type) were fabricated to evaluate the electrochemical properties of SiNT and Si/Ge DLNT electrodes. The precise masses of the Si and Ge were estimated using a microbalance (Sartorius SE2, resolution 1 μg , Sartorius, Germany) before and after the Si and Ge coating process. The electrolyte was a 1.3 M LiPF_6 in a solvent mixture of ethylene carbonate (EC) and diethylene carbonate (DEC) (3:7 vol %). Lithium metal foil was used as a counter electrode. The electrochemical performance testing of SiNT and Si/Ge DLNT electrodes was conducted at a rate of 0.2C between 0.01 and 2 V (TOSCAT 3000, Toyo Systems, Japan). To observe morphological changes of Si/Ge DLNT as a function of amount of lithium insertion, FE-TEM (FE-TEM, JEM 2100F, JEOL, Japan) was employed. All sample preparation was carried out in an argon-filled glovebox to protect oxidation from air and moisture.

The DFT calculations for the adsorption and diffusion energy barriers for Li at SiNT and Si/Ge DLNT were performed using the VASP code.²⁰ The plane-wave basis set was expanded to a cutoff energy of 350.00 eV, and the $4 \times 4 \times 1$ k-point grids of generated by the Monkhorst-Pack scheme were used for the structural relaxations and the total energy calculations of the $2 \times 2 \times 3$ supercells of Si and Ge in the diamond structure.²¹ The projector-augmented waves (PAW) and the generalized gradient approximation (GGA) were used.^{22,23} For the modeling of the Li adsorption and diffusion in SiNT and Si/Ge DLNT, we used ideal six double layers (12 layers) of Si and Ge slabs cut in the [111] crystallographic direction, according to the lowest surface energy of Si and Ge. To avoid the interaction between the adjacent cells in the z-axis direction, 14 Å vacuums were placed above the Si(111) and Ge(111) substrates. Finally, we obtained the energy barriers for the Li atom movements into the first interstitial site, using the nudged elastic band scheme.²⁴

Acknowledgment. This work was financially supported by National Research Foundation of Korea (NRF) through Grant No. K20704000003TA050000310, Global Research Laboratory (GRL) Program provided by the Korean Ministry of Education, Science and Technology (MEST) in 2011, and WCU (World Class University) program through the National Research Foundation of Korea funded by the Ministry of Education, Science and Technology (R31-10092).

Supporting Information Available: Supporting Figures 1–9. This material is available free of charge via the Internet at <http://pubs.acs.org>.

REFERENCES AND NOTES

- Law, M.; Goldberger, J.; Yang, P. D. Semiconductor Nanowires and Nanotubes. *Annu. Rev. Mater. Res.* **2004**, *34*, 83–122.
- Fan, H. J.; Werner, P.; Zacharias, M. Semiconductor Nanowires: From Self-Organization to Patterned Growth. *Small* **2006**, *2*, 700–717.
- Arnold, M. S.; Avouris, P.; Pan, Z. W.; Wang, Z. L. Field-Effect Transistors Based on Single Semiconducting Oxide Nanobelts. *J. Phys. Chem. B* **2003**, *107*, 659–663.
- Goldberger, J.; He, R. R.; Zhang, Y. F.; Lee, S. W.; Yan, H. Q.; Choi, H. J.; Yang, P. D. Single-Crystal Gallium Nitride Nanotubes. *Nature* **2003**, *422*, 599–602.
- Iijima, S.; Ichihashi, T. Single-Shell Carbon Nanotubes of 1-nm Diameter. *Nature* **1993**, *363*, 603–605.
- Cui, Y.; Wei, Q. Q.; Park, H. K.; Lieber, C. M. Nanowire Nanosensors for Highly Sensitive and Selective Detection of Biological and Chemical Species. *Science* **2001**, *293*, 1289–1292.
- Kodambaka, S.; Tersoff, J.; Reuter, M. C.; Ross, F. M. Germanium Nanowire Growth Below the Eutectic Temperature. *Science* **2007**, *316*, 729–732.
- Xiang, J.; Lu, W.; Hu, Y. J.; Wu, Y.; Yan, H.; Lieber, C. M. Ge/Si Nanowire Heterostructures as High-Performance Field-Effect Transistors. *Nature* **2006**, *441*, 489–493.
- Wen, C. Y.; Reuter, M. C.; Bruley, J.; Tersoff, J.; Kodambaka, S.; Stach, E. A.; Ross, F. M. Formation of Compositionally Abrupt Axial Heterojunctions in Silicon-Germanium Nanowires. *Science* **2009**, *326*, 1247–1250.
- Song, T.; Xia, J. L.; Lee, J. H.; Lee, D. H.; Kwon, M. S.; Choi, J. M.; Wu, J.; Doo, S. K.; Chang, H.; Park, W. I.; *et al.* Arrays of Sealed Silicon Nanotubes as Anodes for Lithium Ion Batteries. *Nano Lett.* **2010**, *10*, 1710–1716.
- Graetz, J.; Ahn, C. C.; Yazami, R.; Fultz, B. Nanocrystalline and Thin Film Germanium Electrodes with High Lithium Capacity and High Rate Capabilities. *J. Electrochem. Soc.* **2004**, *151*, A698–A702.
- Yoon, S.; Park, C.-M.; Sohn, H.-J. Electrochemical Characterizations of Germanium and Carbon-Coated Germanium Composite Anode for Lithium-Ion Batteries. *Electrochem. Solid State Lett.* **2008**, *11*, A42–A45.
- Yang, L. C.; Gao, Q. S.; Li, L.; Tang, Y.; Wu, Y. P. Mesoporous Germanium as Anode Material of High Capacity and Good Cycling Prepared by a Mechanochemical Reaction. *Electrochem. Commun.* **2010**, *12*, 418–421.
- Baggetto, L.; Notten, P. H. L. Lithium-Ion (De)Insertion Reaction of Germanium Thin-Film Electrodes: An Electrochemical and *In Situ* XRD Study. *J. Electrochem. Soc.* **2009**, *156*, A169–A175.
- Chan, C. K.; Zhang, X. F.; Cui, Y. High Capacity Li Ion Battery Anodes Using Ge Nanowires. *Nano Lett.* **2008**, *8*, 307–309.
- Seo, M. H.; Park, M.; Lee, K. T.; Kim, K.; Kim, J.; Cho, J. High Performance Ge Nanowire Anode Sheathed with Carbon for Lithium Rechargeable Batteries. *Energy Environ. Sci.* **2011**, *4*, 425–428.
- Timoshenko, S.; Goodier, J. N. *Theory of Elasticity*, 3rd ed.; McGraw-Hill: New York, 1969; p xxiv, 567 pp.
- Armstrong, A. R.; Lyness, C.; Panchmatia, P. M.; Islam, M. S.; Bruce, P. G. The Lithium Intercalation Process in the

- Low-Voltage Lithium Battery Anode $\text{Li}_{1+x}\text{V}_{1-x}\text{O}_2$. *Nat. Mater.* **2011**, *10*, 223–229.
19. Zhang, Q. F.; Zhang, W. X.; Wan, W. H.; Cui, Y.; Wang, E. G. Lithium Insertion in Silicon Nanowires: An *Ab Initio* Study. *Nano Lett.* **2010**, *10*, 3243–3249.
 20. Kresse, G.; Furthmüller, J. Efficient Iterative Schemes for *Ab Initio* Total-Energy Calculations Using a Plane-Wave Basis Set. *Phys. Rev. B* **1996**, *54*, 11169–11186.
 21. Monkhorst, H. J.; Pack, J. D. Special Points for Brillouin-Zone Integrations. *Phys. Rev. B* **1976**, *13*, 5188–5192.
 22. Kresse, G.; Joubert, D. From Ultrasoft Pseudopotentials to the Projector Augmented-Wave Method. *Phys. Rev. B* **1999**, *59*, 1758–1775.
 23. Perdew, J. P.; Chevary, J. A.; Vosko, S. H.; Jackson, K. A.; Pederson, M. R.; Singh, D. J.; Fiolhais, C. Atoms, Molecules, Solids, and Surfaces: Applications of the Generalized Gradient Approximation for Exchange and Correlation. *Phys. Rev. B* **1992**, *46*, 6671–6687.
 24. Henkelman, G.; Uberuaga, B. P.; Jonsson, H. A Climbing Image Nudged Elastic Band Method for Finding Saddle Points and Minimum Energy Paths. *J. Chem. Phys.* **2000**, *113*, 9901–9904.